ARTICLE

Check for updates

Non-thermal Tomonaga-Luttinger liquid eventually emerging from hot electrons in the quantum Hall regime

Kotaro Suzuki[1], Tokuro Hata [1], Yuya Sato[1], Takafumi Akiho[2], Koji Muraki [2] & Toshimasa Fujisawa [1✉]

Dynamics of integrable systems, such as Tomonaga-Luttinger (TL) liquids, is deterministic, and the absence of stochastic thermalization processes provides unique characteristics, such as long-lived non-thermal metastable states with many conserved quantities. Here, we show such non-thermal states can emerge even when the TL liquid is excited with extremely high-energy hot electrons in chiral quantum-Hall edge channels. This demonstrates the robustness of the integrable model against the excitation energy. Crossover from the single-particle hot electrons to the many-body TL liquid is investigated by using on-chip detectors with a quantum point contact and a quantum dot. The charge dynamics can be understood with a single-particle picture only for hot electrons. The resulting electron-hole plasma in the TL liquid shows a non-thermal metastable state, in which warm and cold electrons coexist without further thermalization. The multi-temperature constituents are attractive for transporting information with conserved quantities along the channels.

[1] Department of Physics, Tokyo Institute of Technology, 2-12-1 Ookayama, Meguro, Tokyo 152-8551, Japan. [2] NTT Basic Research Laboratories, NTT Corporation, 3-1 Morinosato-Wakamiya, Atsugi 243-0198, Japan. ✉email: fujisawa@phys.titech.ac.jp

The Coulomb interaction in one-dimensional (1D) conductors plays an essential role in non-equilibrium transport characteristics[1–6]. Two distinct transport regimes, Tomonaga–Luttinger (TL) liquid in the low-energy regime and single-particle hot-electron transport in the high-energy regime, appear in chiral 1D channels of an integer quantum Hall (QH) region at Landau-level filling factor $\nu = 2$ in AlGaAs/GaAs heterostructures[7–9]. In the low-energy regime, the energy dispersion near the Fermi energy can be approximated to be linear and the system is well described with collective excitation modes in the TL liquid model[10,11]. Arbitrary electronic excitation can be represented by spin and charge collective modes. The collective excitations propagate at different velocities for each mode, a phenomenon known as spin-charge separation[12–16]. Owing to the integrable nature of the TL model, the electronic excitation will be equilibrated into an ensemble of spin and charge excitations but not fully relaxed into a thermal equilibrium state[17–21]. This non-thermal metastable state (prethermalized state) survives even after traveling over a distance (>20 μm) much longer than required for the spin-charge separation (<0.1 μm)[22–24]. In these experiments, the initial state is excited with low energies (<0.2 meV from the Fermi energy) where the TL model holds well. The validity of the TL model, or the system's integrability, is no longer guaranteed in the high-energy regime, where due to the deviation from the linear energy dispersion the Coulomb interaction induces weak electron–electron (e–e) scattering between the hot and cold electrons[25,26].

In the high-energy regime, the hot electron travels for a long distance (>10 μm) without losing energy when the Coulomb interaction is suppressed, for example, by screening the interaction with metal on the surface[27–31]. Such ballistic hot electron transport can be seen at high energy (>50 meV) from the Fermi energy. In the intermediate energy region, the e–e scattering becomes significant, where the crossover between the TL liquid and single-particle hot electron transport is expected. However, the crossover regime remained veiled as the cold- and hot-electron dynamics have been studied separately by using different experimental schemes.

Here, we investigate the crossover dynamics from high-energy hot electrons to a non-thermal TL liquid, where the hot electrons lose their energy by exciting the TL liquid under the Coulomb interaction. The resulting state is unusual as warm and cold electrons coexist in the same channel even in the quasi-steady state. The emergence of the non-thermal many-body state is striking as the hot-electron energy is well beyond the low-energy regime for the TL liquid. The obtained non-thermal state is stable for long transport even after full relaxation of hot electrons, which represents the robustness of the integrable nature. We find that the final state depends on the initial hot-electron energy even after the equilibration, while energy-dependent dissipation is observed at higher energy. The crossover includes intra-channel scattering generating a hot spot in the spin-up channel and subsequent inter-channel scattering generating another hot spot in the spin-down channel. The characteristics are experimentally obtained by using a quantum point contact (QPC) as a spin-dependent bolometer to extract the energy-space trajectory of hot electrons and a quantum dot (QD) as a narrow-band spectrometer to evaluate the non-thermal TL liquid. The QH channel is a promising platform to study the interplay between single-particle and many-body physics.

Results and discussion

Crossover dynamics. We investigate the dynamics of hot and cold electrons in the two chiral edge channels at $\nu = 2$ in a high magnetic field B. Figure 1a illustrates our finding on how the energy distribution functions $f_\uparrow$ and $f_\downarrow$ of up and down spins, respectively, change with traveling along the x-axis. With the spin-up and down channels equilibrated with cold electrons prepared at the base temperature T_B at $x < 0$, we inject hot electrons with energy eV_{inj} selectively to the spin-up channel at $x = 0$ [panel (i)]. For moderate eV_{inj}, the Coulomb interaction induces intra-channel e–e scattering between the hot and cold spin-up electrons (e↑–e↑), and electron-hole plasma (the light magenta regions) is generated in the spin-up channel [panel (ii)][26]. We neglect three-body e–e scattering throughout this paper for simplicity[32]. The hot-electron relaxation can be characterized by the energy decay rate per unit length, $\gamma_{\uparrow\uparrow} = -dE_h/dx$, for hot-electron's energy E_h and the maximum energy exchange in a single scattering event, $\Delta E_{\uparrow\uparrow}$[33,34]. $\gamma_{\uparrow\uparrow}$ is obtained by measuring the energy(E_h)-space(x) trajectory of the hot electrons, and $\Delta E_{\uparrow\uparrow}$ is roughly estimated from the spread of the distribution function, W_d, near the chemical potential μ. As we show later, both $\gamma_{\uparrow\uparrow}$ and $\Delta E_{\uparrow\uparrow}$ increase rapidly as the hot electrons lose energy. The resultant sharp drop in the hot electron's energy creates a hot spot at $x = x_{H\uparrow}$, where the spin-up electrons are maximally excited [panel (iii)]. In addition, the inter-channel e–e scattering between up and down spins (e↑–e↓) excites plasma (the dark magenta regions) and creates another hot spot at $x = x_{H\downarrow}$ in the spin-down channel [panel (iv)]. The e↑–e↓ scattering equilibrates the two channels further during transport. Importantly, once the electron-hole plasma relaxes to fit in the energy range where the TL physics governs, the plasma cannot equilibrate further and remains in a non-thermal metastable state in which warm and cold electrons coexist in the same channel [panel (v)]. Such crossover from hot electrons into a non-thermal TL liquid is the subject of this paper. Due to the coupling to the environment, the system finally reaches thermal equilibrium at T_B after long transport [panel (vi)].

The crossover dynamics can be understood by considering microscopic processes in the edge states, where the Landau levels are bent upwards by the edge potential, as schematically shown in Fig. 1b. This energy(E)–space(y) diagram can be understood with the energy(E)–wavenumber(k_x) dispersion, as the relation $k_x = -eBy/\hbar$ holds in the QH regime under the Landau gauge[7]. Due to the nonlinearity of the dispersion, e–e scattering is suppressed as it cannot conserve both energy and momentum, particularly when the energy E_h and the energy exchange ε are large (Fig. 1c). In reality, the scattering is allowed by the presence of disorder that breaks the translational invariance and lifts the momentum conservation to some extent. This should determine the cut-off $\Delta E_{\uparrow\uparrow}$ in the e–e scattering. For the concave dispersion relation, $\Delta E_{\uparrow\uparrow}$ should increase with decreasing E_h. The Coulomb interaction increases with decreasing the distance at lower E_h. Both effects induce the rapid reduction of E_h with large $\gamma_{\uparrow\uparrow}$ and $\Delta E_{\uparrow\uparrow}$ near $x = x_{H\uparrow}$.

When $E_h < \Delta E_{\uparrow\uparrow}$ is reached, the system enters a new regime, where the scattering involves two competing processes with the swapped final states (the dashed lines with an arrow labeled e↑–e↑ in Fig. 1d). They destructively interfere with each other, and thus the intra-channel scattering of the same spins should be suppressed at low E_h (<$\Delta E_{\uparrow\uparrow}$)[34]. When the intra-channel scattering is inefficient, the inter-channel scattering between different spins should dominate the relaxation. This region can be referred to as the inter-channel scattering regime. The hot electrons in the spin-up channel lose their energies by exciting an electron-hole plasma in the spin-down channel, and no competing process is present for scattering between different spins. The inter-channel scattering subsequently excites the spin-up channel and thus equilibrates the two channels in the end. As the spin-down channel is located on the inner side, where the edge potential is more gentle, the maximum energy exchange
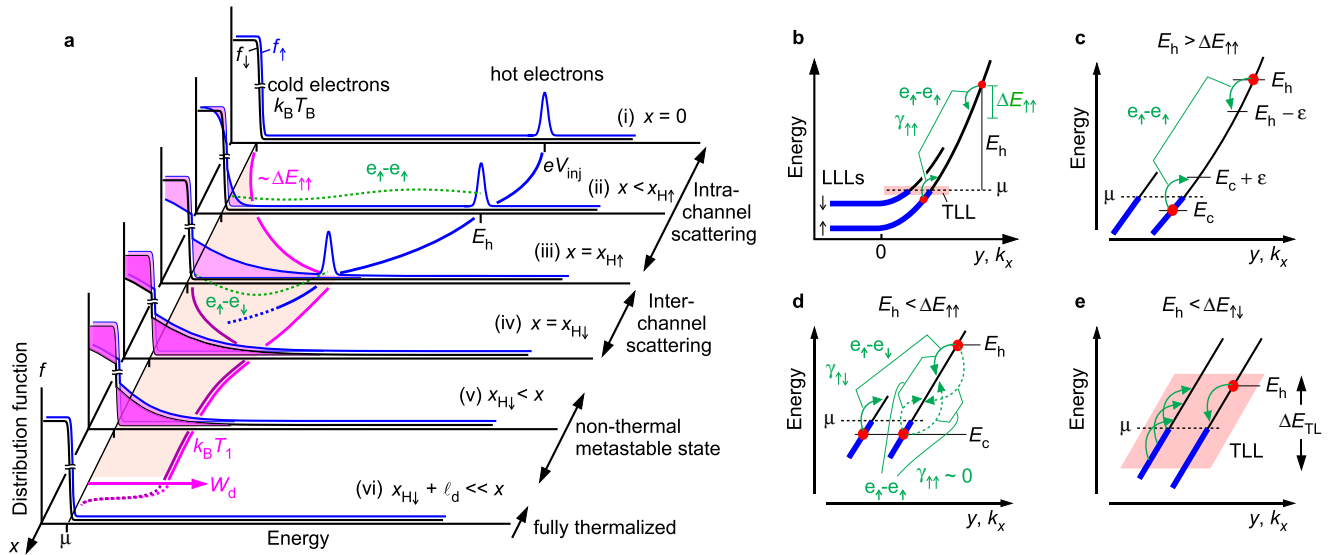
Fig. 1 Crossover dynamics of single-particle scattering processes and non-thermal Tomonaga–Luttinger (TL) liquid. a Schematic spatial evolution of energy distribution functions $f_\uparrow$ and $f_\downarrow$ for up- and down-spins, respectively. Hot electrons are injected into the spin-up channel at energy eV_{inj} (i) and relax with intra-channel electron–electron scattering ($e_\uparrow$-$e_\uparrow$) and inter-channel scattering ($e_\uparrow$-$e_\downarrow$) (i)-(iv). Electron-hole plasma is excited in the channels, and hot spots appear at $x_{H\uparrow}$ and $x_{H\downarrow}$ in the spin-up and -down channels, respectively. The system ends up in a non-thermal metastable state (v) before reaching thermal equilibrium (vi). **b** Energy profiles for the lowest Landau levels (LLLs) for up and down spins. Intra-channel electron–electron scattering ($e_\uparrow$-$e_\uparrow$) is shown for a hot electron at energy E_h. **c** Intra-channel scattering ($e_\uparrow$-$e_\uparrow$) for hot and cold electrons at energies E_h and E_c, respectively, and final states at $E_h - \varepsilon$ and $E_c + \varepsilon$ with energy exchange ε. **d** Inter-channel scattering ($e_\uparrow$-$e_\downarrow$) and suppressed intra-channel scattering ($e_\uparrow$-$e_\uparrow$) with destructive interference for $E_h < \Delta E_{\uparrow\uparrow}$. **e** Formation of a TL liquid within the energy range ΔE_{TL}.
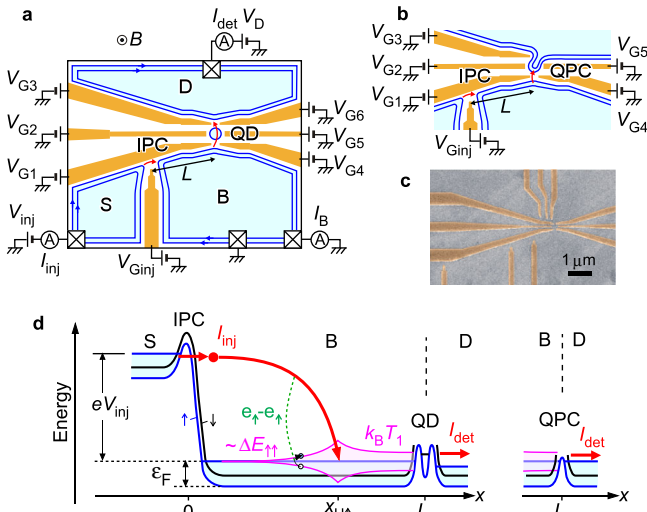

Fig. 2 Schematic measurement setup. a Device structure. By applying gate voltages on the gates (yellow), an injector point contact (IPC) and a detector quantum dot (QD) are formed between the source (S), base (B), and drain (D) regions. The blue parallel lines show edge channels at $\nu = 2$. **b** Device configuration for a quantum point contact (QPC) detector. **c** Scanning electron micrograph with the false color of a control device with several IPC gates. **d** Schematic energy diagram of the measurement. Electrons are filled with the Fermi energy ε_F for up- and down-spin channels. The energy-space trajectory of hot electrons is shown by the red arrows. Electron-hole plasma near the chemical potential in B is analyzed by measuring I_{det} through the QD or QPC.

$\Delta E_{\uparrow\downarrow}$ and the energy loss rate $\gamma_{\uparrow\downarrow}$ for different spins should be smaller than $\Delta E_{\uparrow\uparrow}$ and $\gamma_{\uparrow\uparrow}$, respectively.

The above single-particle picture fails when the hot electron is further relaxed within the energy range ΔE_{TL} of the TL regime ($E_h \lesssim \Delta E_{TL}$). The dispersion can be approximated to be linear, as

shown in Fig. 1e. All electrons within the energy range ΔE_{TL} near the Fermi level interact with each other. Such interacting electrons can be understood with non-interacting bosonic excitations in the TL model[10,20]. The inter-channel interaction induces spin-charge separation, and the intra-channel interaction enhances the charge velocity.[16] Once all electron-hole plasma enters the TL regime, no further transformation is expected in the plasma. Therefore, a non-thermal metastable state eventually shows up after stochastic processes. In the following experiment, the coexistence of warm and cold electrons remains even after long-distance transport. While the TL model is based on low-energy physics, such non-thermal states can emerge from high-energy hot electrons. This demonstrates the robustness of the prethermalized state against the excitation energy.

Electronic distribution functions of non-thermal states have been studied previously. When an initial state with a double-step distribution function is prepared by a QPC with bias voltage V_b and low transmission probability, the non-thermal state shows an arctangent distribution function in the low-energy limit at $|E - \mu| \ll eV_b$[21,23]. Phenomenologically, the non-thermal states in the high-energy region can be approximated by a binary distribution function:

$$f(E) = (1 - p)f_{FD}(E; k_B T_0) + pf_{FD}(E; k_B T_1) \quad (1)$$

consisting of high- (T_1) and low-temperature (T_0, close to the base temperature T_B) components with Fermi distribution $f_{FD}(E; k_B T) = 1/[1 + \exp(E/k_B T)]$, which is valid for small fraction p ($\ll 1$)[22]. The binary form captures the exponential current profiles $\sim e^{-E/k_B T_1}$ observed in the low-energy regime[22–24]. As we do not know the theoretical form for hot-electron injection, we use this binary form to analyze the non-thermal states in this paper.

Experimental setup. We investigated the crossover dynamics with the device fabricated in a standard AlGaAs/GaAs heterostructure with an electron density of 2.5×10^{11} cm^{-2} and

low-temperature mobility of about 10^6 cm²/Vs, as shown in Fig. 2a. The electron system is divided into three conductive regions that serve as the source (S), base (B), and drain (D) by applying large negative gate voltages V_{Gi} on gate $i = 1, 2, 3, \cdots$. A perpendicular magnetic field $B = 5.0$ T is applied to set the electron system in the $\nu = 2$ QH regime and form two parallel edge channels (the blue lines) in each region.

Hot electrons with up spin and energy eV_{inj} ($=1 - 100$ meV) are injected from S to B, by applying voltage $-V_{inj}$ to the ohmic contact of S and tuning the transmission of the injector point contact (IPC). The electronic distribution function of the up-spin channel near the chemical potential is investigated with a QD, and electron-hole plasma in up- and down-spin channel are studied by activating a QPC as shown in Fig. 2b. The QD or QPC is located at a distance L from the IPC, where several injection gates at different distances $L = 1, 2, 5, 10, 20$, and 30 μm were selectively activated (see the scanning electron micrograph of Fig. 2c). As shown in the schematic energy profile of Fig. 2d, the hot spot ($x_{H\uparrow}$) can be changed by tuning eV_{inj}. The non-thermal state in the TL regime can be investigated at $x = L > x_{H\uparrow}$, and e–e scattering processes can be studied at $x = L < x_{H\uparrow}$. The current I_{det} through the QD or QPC is measured with a bias voltage V_D on the detector (D) ohmic contact. The base current I_B is monitored to ensure $I_{inj} \simeq I_{det} + I_B$ (see Supplementary Fig. 1).

Energy-space trajectory of hot electrons. First, we investigate the hot-spot positions $x_{H\uparrow}$ and $x_{H\downarrow}$ by using QPC detection[26,35]. As shown in Fig. 3a, the QPC conductance G obtained without injecting hot electrons (by opening the IPC with $V_{inj} = 0$ and $V_{Ginj} = 0$) shows standard quantized conductances as a function of the gate voltage V_{G4}. The onsets for spin-up and -down transport are seen at $V_{G4} \sim -0.4$ V and -0.2 V, respectively. Additional peaks at $V_{G4} \sim -0.5$ V are associated with parasitic impurity states, which play minor roles in the following analysis. The following QPC detection was performed at $V_D = 0$. When hot spin-up electrons at energy eV_{inj} are injected from the IPC for $L = 1$ μm, distinct features appear in the detector current profile I_{det}, as shown in Fig. 3b. For the bottom trace at small $eV_{inj} = 2$ meV, a single current step with a height comparable to
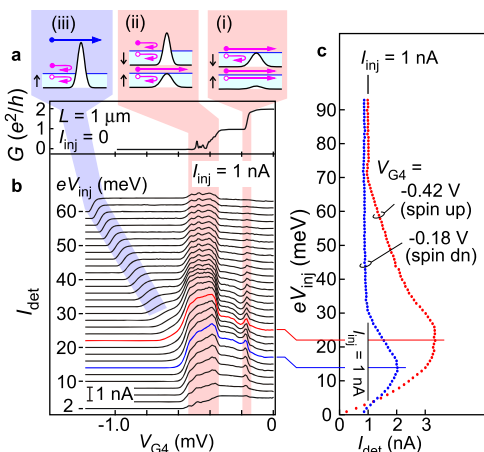
$I_{inj} = 1$ nA is seen at the opening of the spin-up transport ($V_{G4} \sim -0.4$ V). This ensures no tunneling between spin-up and -down channels. With increasing eV_{inj}, current peaks (rather than steps) show up for both spin-up and -down transports (in the pink stripes). As shown in the insets (i) and (ii) to Fig. 3a, each peak can be understood by considering the bolometric detection for each channel, where higher-energy electrons are transmitted but lower-energy holes are reflected[26]. Therefore, the peak current is proportional to the density of the electron-hole plasma in the respective channel, while the sensitivity for up spins may be greater than that for down spins. Since the hot spot is the point where the detected current is maximal, the strategy to determine the hot spot position (for a given L) is to look for the voltage V_{inj} that maximizes the detected current. The peak currents for up spins ($V_{G4} = -0.42$ V) and down spins ($V_{G4} = -0.18$ V) are plotted as a function of eV_{inj} in Fig. 3c. The spin-up current is maximized at $eV_{inj} = 22$ meV, which indicates that the position of the hot spot in the spin-up channel coincides with that of the QPC detector ($x_{H\uparrow} = 1$ μm for $eV_{inj} = 22$ meV). Similarly, the spin-down current is maximized at $eV_{inj} = 14$ meV, where the hot spot in the spin-down channel is considered to be located at the position of the QPC detector ($x_{H\downarrow} = 1$ μm for $eV_{inj} = 14$ meV).

We repeated similar measurements for various L, and the obtained hot-spot positions are summarized in Fig. 4a. In addition to the data obtained with the QPC (the circles), data obtained with the QD only for spin-up (described below) are also plotted by the squares. Both data for up spins agree well with each other within the experimental reproducibility. The smooth connection of the data points can be used to extract the energy-space trajectory of hot electrons. $\gamma_{\uparrow\uparrow}$ can be obtained from $\gamma_{\uparrow\uparrow} = d(eV_{inj})/dL$, as the hot spot $x_{H\uparrow}$ ($=L$) increases with eV_{inj} at rate $\gamma_{\uparrow\uparrow}^{-1}$. Empirically, the power-law dependence in a form of

Fig. 3 Quantum point contact (QPC) detection of electron-hole plasma.
a Conductance $G = I_{det}/V_D$ of the detector QPC measured with $V_D = 0.1$ mV. Transmission and reflection of hot electrons (the blue arrow) and cold electrons and holes (the magenta arrows) are illustrated in the insets (i), (ii), and (iii). **b** I_{det} profiles obtained at various eV_{inj}. V_{G4} in the horizontal axis was simultaneously swept with V_{G5} ($=V_{G4}$). **c** The peak current of I_{det} for spin-up (red) and -down (blue) are plotted as a function of eV_{inj}. The maximum peak current appears when the hot spot is located close to the detector.
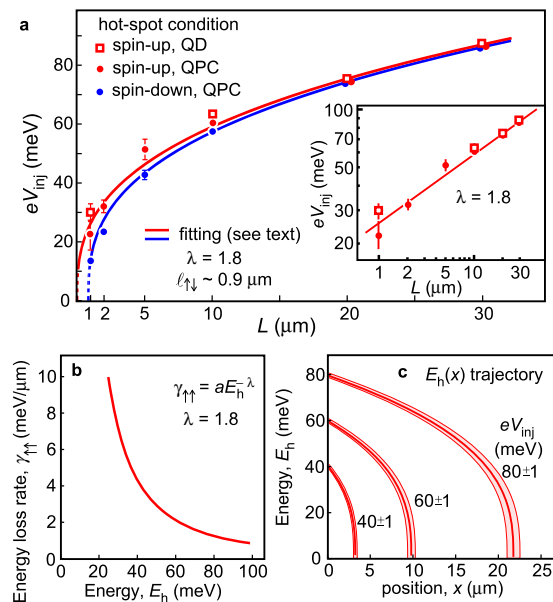

Fig. 4 Energy-space trajectory of hot electrons. a The hot-spot conditions for up (red) and down (blue) spins measured with quantum point contact (QPC) (circles) and quantum dot (QD) (squares) detectors. The error bar shows the variations due to the injector and detector conditions. The solid lines are fitted to the data with $\lambda = 1.8$ (the uncertainty between 1.6 and 2.2) and $\ell_{\uparrow\downarrow} = 0.9$ μm. The inset shows the data in the double logarithmic plot. **b** The estimated energy loss rate $\gamma_{\uparrow\uparrow}$ by assuming the power dependence of hot-electron energy E_h. **c** The estimated energy(E_h)-space(x) trajectory of hot electrons for $eV_{inj} = 40, 60$, and 80 meV. Each stripe represents the spread associated with variation of eV_{inj} by ±1 meV.

$\gamma_{\uparrow\uparrow} = aE_{h}^{-\lambda}$ for hot-electron energy E_h explains the data with parameters a and λ[26]. This suggests an energy(E_h)-space(x) trajectory:

$$E_{h}(x) = [(eV_{inj})^{\lambda+1} - a(\lambda+1)x]^{1/(\lambda+1)}, \qquad (2)$$

and the hot-spot condition:

$$eV_{inj} = [a(\lambda+1)x_{H\uparrow}]^{1/(\lambda+1)}. \qquad (3)$$

The latter reproduces our data very well with $\lambda = 1.8$, as shown by the red curve in Fig. 4a. Corresponding energy loss rate $\gamma_{\uparrow\uparrow}(E_h)$ increases with decreasing E_h, as shown in Fig. 4b. The energy-space trajectory $E_h(x)$ is shown for several eV_{inj} values in Fig. 4c. As the energies of incident electrons should be distributed at around eV_{inj} mostly due to the energy-dependent tunneling probability of the IPC, possible dispersion of the trajectories for ±1 meV distribution is shown by pink stripes. Notice that hot-electron relaxation proceeds rapidly just before the hot spot $x_{H\uparrow}$, which can be tuned with V_{inj}. This is useful for investigating the decay length of non-thermal states, as one can change the distance D between the hot spot and the detector.

As for the spin-down hot spot $x_{H\downarrow}$ shown by the blue circles in Fig. 4a, the L dependence can be reproduced by the blue curve which is obtained just by shifting the red curve horizontally by $\ell_{\uparrow\downarrow} = 0.9$ μm. This suggests that finite length $\ell_{\uparrow\downarrow}$, independent of eV_{inj}, is required for exciting spin-down electrons through the inter-channel interaction. This $\ell_{\uparrow\downarrow}$ is much longer than the length l_{SC} required for spin-charge separation in the TL regime. Similar devices show $l_{SC} \simeq 0.18$ μm at $eV_{inj} = 0.6$ meV, and l_{SC} decreases with increasing eV_{inj} ($l_{SC} \propto 1/V_{inj}$)[23]. The difference $(\ell_{\uparrow\downarrow} > l_{SC})$ indicates the existence of the stochastic inter-channel e–e scattering regime between $x_{H\uparrow}$ and $x_{H\downarrow}$.

The transition between intra- and inter-channel scattering regimes can be confirmed from the data in Fig. 3c. In the range of eV_{inj} between 30 and 70 meV for $L < x_{H\uparrow}$, spin-up electrons are highly excited ($I_{det} > I_{inj}$) but no spin-down electrons are excited ($I_{det} \simeq I_{inj}$) because the intra-channel scattering is dominant. In contrast, both signals become large at $eV_{inj} < 25$ meV and change in a similar manner at $eV_{inj} < 15$ meV ($L > x_{H\downarrow}$), where the inter-channel interaction equilibrates the two channels. The sequence of the intra-channel scattering regime [from (i) to (iii) in Fig. 1a] followed by the inter-channel scattering regime [(iii)–(iv)] is justified with the result.

QD spectroscopy

We investigate electronic excitation in the spin-up channel by using the QD detector[23,36]. Coulomb diamond characteristics of the QD are shown in Supplementary Fig. 2. Figure 5a shows the Coulomb blockade (CB) oscillations obtained with $V_D = 0.2$ mV under hot-electron injection at $L = 10$ μm. The horizontal axis ΔV_{G5} is the relative voltage of V_{G5} from the left onset of the right CB peak. The width of the CB peaks in the bottom trace measures the transport window of eV_D. When hot electrons are injected at various eV_{inj} and fixed $I_{inj} = 1.8$ pA, excess current appears in the entire CB region, as highlighted by the pink color. This current measures the electrons excited above the QD level. For instance, the current at $\Delta V_{G5} = -19$ mV (the dashed line) becomes maximum at $eV_{inj} = 62$ meV, as shown in Fig. 5b. This measures the spin-up hot-spot condition, where the hot electrons injected at $eV_{inj} = 62$ meV just relaxed to the Fermi energy at $L = 10$ μm. This coincides with the QPC data, as shown by the squares in Fig. 4a. In the following analysis, we use the hot-electron trajectory given by Eq. (2) at $\lambda = 1.8$, while the parameter a for each geometry (L) is determined from eV_{inj} that maximizes I_{det} by using Eq. (3).
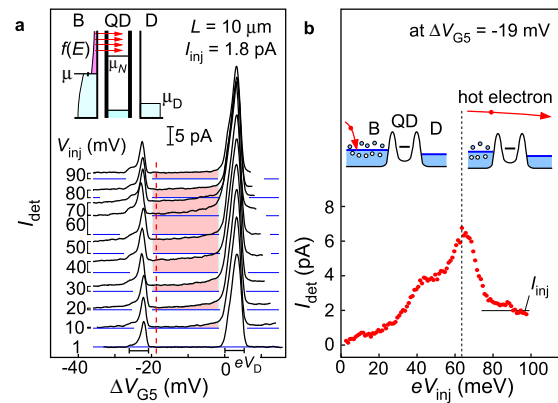

Fig. 5 Quantum dot (QD) detection of electron-hole plasma. a Coulomb oscillations of the QD observed in detector current I_{det} as a function of relative gate voltage ΔV_{G5} under hot-electron injection at various injection voltage V_{inj}. The excess current is highlighted by the pink color. The inset shows the energy diagram of the QD. **b** I_{det} measured in the deep Coulomb blockade (CB) region at $\Delta V_{G5} = -19$ mV (the dashed line in **a**). The left inset shows the energy diagram for $eV_{inj} \lesssim 60$ meV, where the hot electrons relax before reaching the QD. The right inset shows the diagram for $eV_{inj} \gtrsim 60$ meV, where the hot electrons pass over the QD.

The broad current profile in Fig. 5a suggests that the electrons are excited well above the charging energy of the QD ($U \simeq 1.5$ meV) as well as the single-particle energy spacing of the QD ($\bar{\Delta} \simeq 0.2$ meV on average). The current decreases with decreasing ΔV_{G5} reflecting the electron energy distribution function $f(E)$ of the channel. To evaluate $f(E)$, the current profiles are plotted in the logarithmic scale in Fig. 6a for $eV_{inj} \leq 60$ meV, where the hot electrons are fully relaxed before reaching the QD detector ($x_{H\uparrow} < L$). The current profile in the CB region shows exponential dependence $I_{det} \propto \exp(\alpha \Delta V_{G5}/W_c)$ as shown by the dashed lines. Here, $\alpha \simeq 0.044e$ is the lever arm factor to convert ΔV_{G5} into the electrochemical potential $\mu_N = -\alpha \Delta V_{G5}$ of the N-electron QD, and W_c is the characteristic energy of the current profile. For $eV_{inj} > 62$ meV, the hot electrons pass over the QD potential ($x_{H\uparrow} > L$), as shown in the inset to Fig. 6b. Noting that all the hot electrons are eventually absorbed by the ammeter, we plot in Fig. 6b $I_{det} - I_{inj}$ as the net current in the logarithmic scale. The exponential profile, $\propto \exp(\alpha \Delta V_{G5}/W_c')$, in the CB region is characterized by W_c'. We confirmed that W_c and W_c' do not change significantly with I_{inj}, as shown in Fig. 6c, d, as well as N (partially seen at $\Delta V_{G5} < -30$ mV in Fig. 6a, b). Some other data obtained at different L and I_{inj} are shown in Supplementary Fig. 3.

To analyze the exponential tail in the CB region, we rely on the orthodox CB theory with a continuous density of QD states[37], as all features associated with the excited states of the QD are smeared out by the broad profile. We also assume the QD is relaxed to the ground state before accepting a single hot-electron. Under these assumptions, the detector current yields:

$$I_{det} = \int_{\mu_N}^{\infty} \frac{G_{QD}}{e} f(E) dE \qquad (4)$$

with G_{QD} the tunneling conductance (see "Methods"). If $G_{QD} \propto e^{E/W_t}$ increases exponentially with energy E at characteristic energy W_t of the tunneling, the model suggests exponential energy dependence of the distribution function $f(E) \propto \exp(-E/W_d)$ with $W_d^{-1} = W_t^{-1} + W_c^{-1}$. While we do not know W_t of our device, the spread of the current tail (W_c) should reflect the spread of the distribution function (W_d) when W_c is not too large.
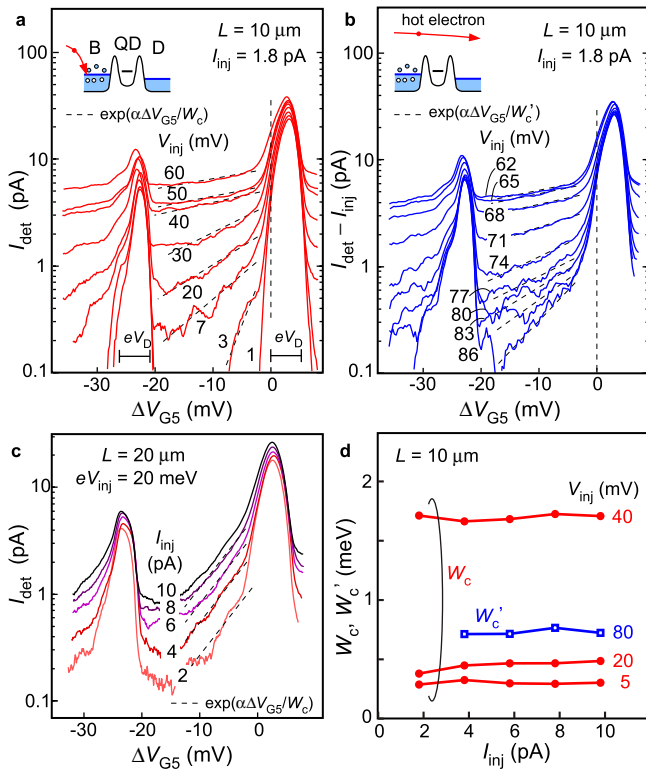
Fig. 6 Quantum dot (QD) spectroscopy for energy distribution functions. **a** Detector current I_{det} as a function of relative gate voltage ΔV_{G5} at various injection energy $eV_{inj} \leq 60$ meV for studying non-thermal metastable states after long transport. **b** Excess current $I_{det} - I_{inj}$ for $eV_{inj} \geq 62$ meV for studying non-equilibrium states in the course of electron–electron scattering. The dashed lines, $\propto \exp(\alpha \Delta V_{G5}/W_c)$ in (**a**) and $\propto \exp(\alpha V_{G5}/W_c')$ in (**b**), are fitted to the data. The current tails in (**a**) and (**b**) are characterized by cut-off energies W_c and W_c', respectively. The insets show the energy diagrams around the QD. **c** I_{det} for several injection current I_{inj} at $eV_{inj} = 20$ meV. No significant change in the slope (the dashed lines) is seen. **d** Injection current I_{inj} dependence of cut-off energies W_c (red) and W_c' (blue).

Non-thermal metastable state. The state after equilibration at $x > x_{H\downarrow}$ can be studied with the data in Fig. 6a. The coexistence of the small exponential current tail with large W_c and the large CB current peak with a sharp onset associated with cold electrons manifests the non-thermal metastable state of the TL liquid[22–24]. In the present case, the non-thermal states are analyzed with the binary form of Eq. (1). The low temperature (T_0) is always close to the base temperature (T_B), as the CB peak remains sharp at any V_{inj} in Fig. 6a. The high temperature (T_1) is related to the spread of the current tail ($k_B T_1 \sim W_c$). Significantly different temperatures ($T_1 \gg T_0$) are seen at higher V_{inj}. These current profiles are qualitatively the same as those reported for small excitation energies (10–100 μeV) where the low-energy TL physics governs. Surprisingly, low-energy physics emerges from the high-energy source (1–60 meV). Note that the non-thermal metastable state is distinct from the ordinary non-equilibrium state often seen in higher dimensions[38,39].

As several QD levels are involved in the transport for the highly non-equilibrium state, p in Eq. (1) cannot be estimated from the current profile. Instead, p can be obtained from the electrical power $P_{inj} = I_{inj} V_{inj}$ injected from the IPC. It is known that a single edge channel carries heat current $J = \frac{\pi^2}{6h}(k_B T)^2$ if the electrons are in thermal equilibrium at temperature T[40]. Therefore, if the spin-up and -down channels were thermally
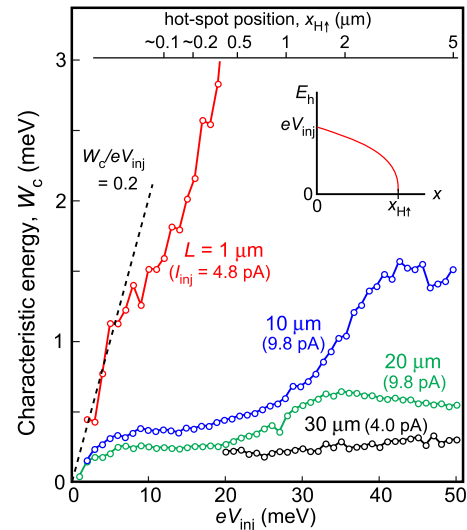

Fig. 7 The cut-off energy W_c for the non-thermal states. The dashed line shows the linear relation, $W_c \simeq 0.2eV_{inj}$, obtained in the low-energy limit of Tomonaga–Luttinger (TL) liquids. The inset shows the energy-space trajectory of hot electrons. The hot-spot position, $x_{H\uparrow}$, obtained with Eq. (3) at $\lambda = 1.8$ is shown in the upper scale.

equilibrated with P_{inj}, the thermal energy would increase to $k_B T_{th} = \sqrt{\frac{3h}{\pi^2} P_{inj}}$ by neglecting the thermal energy of the base temperature (T_B). This yields $k_B T_{th} = 10$ μeV for $P_{inj} = 13$ fW ($I_{inj} = 1.8$ pA and $V_{inj} = 7$ mV), which is much smaller than $W_c = 0.3$ meV at $V_{inj} = 7$ mV for the third trace from the bottom in Fig. 6a. The heat conservation suggests that only a small fraction, about $p = (k_B T_{th}/W_c)^2 \simeq 10^{-3}$ of electrons, is highly excited to the high-temperature T_1. Such an unusual energy distribution is a consequence of the crossover from hot electrons.

The exponential current tail in Fig. 6a starts to develop from $eV_{inj} \simeq 2$ meV, and the corresponding W_c value rapidly increases with eV_{inj}. The W_c values obtained at various eV_{inj} and L are summarized in Fig. 7. First, we focus on the low eV_{inj} ($\lesssim 8$ meV) regime for the shortest $L = 1$ μm, where W_c increases linearly with eV_{inj} (the dashed line). As the hot electron relaxes within a short propagation length ($x_{H\uparrow} < 0.1$ μm as shown in the auxiliary scale) in this case, the distribution function should measure the non-thermal metastable state after traveling of ~1 μm. Actually, the slope $W_c/eV_{inj} = 0.2$ is comparable to the values obtained in the low-energy limit of the TL regime ($W_c/eV_{inj} = 0.17$ for $W_c = 34$ μeV at $eV_{inj} = 200$ μeV with QPC injection in ref. [23], $W_c/eV_{inj} = 0.22$–0.25 for $W_c = 14$–17 μeV at $eV_{inj} = 63$ μeV with QD injection in ref. [24], and $W_c/eV_{inj} = 0.17$ for $W_c = 20$–35 μeV at $eV_{inj} = 100$–200 μeV with indirect QPC injection in ref. [22]). Our experiment confirms that the same ratio (W_c/eV_{inj}) holds up to $W_c \simeq 1$ meV, which is more than ten times greater than the values in the previous works. The linearity implies that the injection energy fits in the energy range of the TL liquid without experiencing e–e scattering. All electrons within the range interact with each other to form the collective plasmon mode, as discussed in Fig. 1e. The memory of the initial state at eV_{inj} remains in the broad electronic distribution function with W_d ($\simeq W_c \simeq 0.2eV_{inj}$). This can be understood with the integrable nature of holding many conserved quantities.

However, W_c deviates from the linear dependence to lower values at $eV_{inj} \gtrsim 8$ meV for $L = 1$ μm, as seen in Fig. 7. W_c obtained with longer L may follow the linear dependence at small $eV_{inj} \lesssim 1$ meV and becomes substantially smaller at larger eV_{inj}.
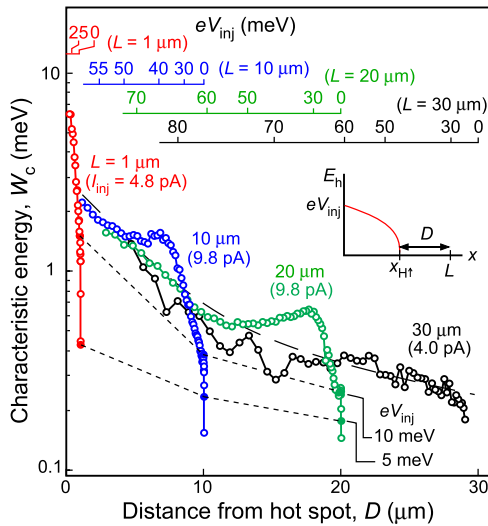
Fig. 8 Decay of non-thermal metastable states. The characteristic energy W_c is plotted as a function of the distance D from the hot spot to the quantum dot (QD). D is obtained from Eq. (3) at $\lambda = 1.8$. The inset shows the energy-space trajectory. The eV_{inj} value for each L is shown in the respective auxiliary scale. The decay of W_c is shown by the short dashed lines connecting the data points obtained with the same eV_{inj} (≤ 10 meV) and the long dashed line as a guide to the eye for the data at $eV_{inj} \gtrsim 50$ meV.

The reduction in W_c might originate from the dissipation[41,42] or the departure from the TL regime. To characterize the decay of non-thermal states, the W_c data are plotted as a function of the distance $D = L - x_{H\uparrow}$ from the hot spot to the detector, as shown in Fig. 8. The corresponding eV_{inj} values are shown in the auxiliary scale for each L. Each trace features a gradual reduction of W_c (except for $L = 1$ μm) at $eV_{inj} > 50$ meV followed by a sudden reduction at $eV_{inj} < 10$ meV ($D \simeq L$). Both features can be explained consistently with the energy-dependent dissipation during traveling.

For $eV_{inj} < 10$ meV, the electron-hole excitation at the hot spot is developing with increasing eV_{inj}, while D ($\simeq L$) is almost constant for each L. Therefore, the dissipation can be studied by varying L for a given eV_{inj}, as shown by the two dotted lines connecting the data points for $eV_{inj} = 5$ and 10 meV. The steeper slope at higher W_c suggests increased dissipation at higher excitation energy.

In contrast, the excitation at the hot spot does not increase further for $eV_{inj} > 30$ meV. As seen in the energy-space trajectory of Fig. 4c, the excess energy beyond 20–30 meV is lost during the long-distance transport with the remaining 20–30 meV used to build the hot spot with the highest excitation energy. Therefore, the eV_{inj} dependence at $eV_{inj} > 30$ meV in Fig. 8 should be understood as representing the D dependence of W_c. The overall feature at $eV_{inj} > 50$ meV follows a monotonic reduction of W_c with D, as shown by the long dashed line. This slope is comparable to the slope of the short-dashed lines if the data in the same range of W_c are compared. The data shows how the electronic distribution function changes with transport. The characteristic energy W_d ($\simeq W_c$) decays fast if W_d is large (the decay length $\ell_d \sim 5$ μm at $W_c \simeq 1$ meV), but the decay length becomes longer for smaller W_d (~ 30 μm at 0.2 meV). This is comparable to $\ell_d \sim 20$ μm obtained from the low-energy experiment at $W_c = 34$ μeV[23]. The energy dependent ℓ_d may be explained by energy-dependent dissipation associated with the characteristics of the environment. If the reduction signifies the departure of the TL regime, the energy range for the TL physics could be $\Delta E_{TL} \sim 1$ meV in our device.
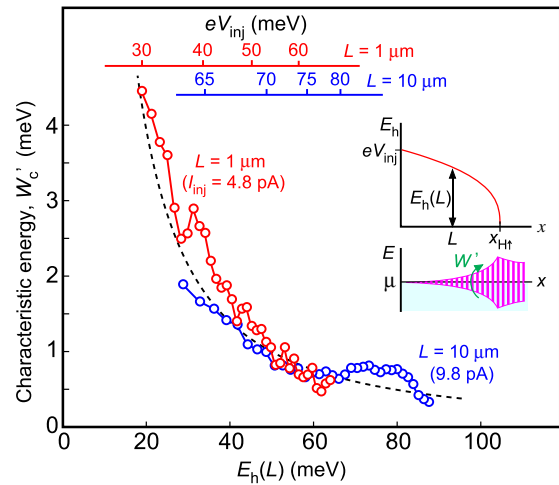

Fig. 9 The characteristic energy W'_c for the electron–electron scattering. The hot-electron energy $E_h(L)$ at the quantum dot (QD) detector is obtained from Eq. (2) at $\lambda = 1.8$. The eV_{inj} value for each L is shown in the respective auxiliary scale. The dashed line is a guide to the eye by using a function proportional to $E_h^{-1.5}$. The inset shows the energy-space trajectory and buildup of electron-hole plasma.

e–e scattering. The electron-hole plasma generated in the course of the e–e scattering was analyzed with the current profile, $I_{det} - I_{inj}$, at $x_{H\uparrow} > L$, in Fig. 6b. The data indicates that W'_c (the inverse of the slope) decreases with increasing eV_{inj}. Considering that the energy loss rate $\gamma_{\uparrow\uparrow}$ increases as E_h decreases during the transport from the IPC to the detector (see Fig. 4b), it is likely that the obtained W'_c value reflects most sensitively the e–e scattering near the detector QD. From this point of view, we plot in Fig. 9 W'_c as a function of $E_h(L)$, the hot-electron energy at the detector position. The two data sets for $L = 1$ and 10 μm show similar dependency, which justifies this approach. The data show that W'_c decreases with increasing E_h, as shown by the dashed line. Namely, the electron-hole plasma is highly excited in the vicinity of the hot spot, as illustrated in the inset.

The physical meaning of W'_c can be understood by considering the electron-hole generation process. Suppose that an intra-channel e–e scattering between a hot electron with energy E_h and a cold electron with E_c (<0) generates an electron-hole pair with a hole at E_c and an electron near the Fermi energy [at $E_c + \varepsilon$ (>0)] by the energy exchange ε, as shown in Fig. 1c. Scattering with various combinations of E_c and ε induces the plasma. Here, ε is bounded by the momentum conservation. For a given E_h, we assume that the scattering probability $P(E_c, \varepsilon; E_h) \propto e^{-\varepsilon/\Delta E_{\uparrow\uparrow}}$ for E_c and ε depends only on ε with the upper bound $\Delta E_{\uparrow\uparrow}$ that depends on E_h. For the present case, we are interested in the electronic energy distribution function $f(E)$ above the Fermi energy ($E > 0$). We further assume that $f(E)$ is determined by the e–e scattering in the vicinity of the detector by neglecting the scattering that occurs in the upstream region. Then, $f(E)$ is given by the instantaneous e–e scattering with E_h at $x = L$ as:

$$f(E) \propto \int_{-\infty}^{0} P(E_c, \varepsilon; E_h) dE_c \propto e^{-E/\Delta E_{\uparrow\uparrow}}, \qquad (5)$$

where $E = E_c + \varepsilon$ was used in the integration. Therefore, provided that W'_c measures the spread W_d of the distribution function, the obtained W'_c can be understood as the energy cut-off $\Delta E_{\uparrow\uparrow}$ of the intra-channel e–e scattering.

The monotonic reduction of W'_c with $E_h(L)$ in Fig. 9 is consistent with the concave dispersion in Fig. 1b, as explained above. In this way, the energy loss of hot electrons ($E_h > 20$ meV)

and excitation of cold electrons ($E_h < 5$ meV) are consistently explained with the intra-channel e–e scattering. It should be noted that the energy dependency (larger W'_c for smaller E_h) of e–e scattering in Fig. 9 is opposite to that (larger W_c for larger eV_{inj}) for TL states in Fig. 7.

Conclusions

We have investigated how high-energy hot electrons lose their energy by exciting cold electrons. A QPC was used as a broadband spin-dependent bolometer to extract the energy-space trajectory of hot electrons. A QD was employed as a narrow-band spectrometer to detect non-equilibrium electronic excitation near the Fermi energy. The hot electrons lose their energy with the e–e scattering and eventually create spin-dependent hot spots. The cold electrons are maximally excited at the hot spot and equilibrate while traveling the channels. Interestingly, the system always ends up with a non-thermal metastable state without fully relaxing into thermal equilibrium, even when the initial hot-electron energy is well beyond the TL regime. This demonstrates the robustness of non-thermal states against the excitation energy. The non-thermal state depends on the excitation energy even after traveling 20 μm. This suggests that the final state remembers the initial state even after the equilibration, in consistency with the integrable nature with many conserved quantities. In addition, the non-equilibrium state generated with the e–e scattering is in-situ investigated to evaluate the maximum energy exchange in the scattering. The analysis implies the significance of inter-channel scattering with different spins as well as intra-channel scattering with the same spins. The experiment provides a novel crossover from single particles to a non-equilibrium many-body state. The scheme can be used for studying non-linear TL liquids in the presence of non-linear dispersion[43]. The robustness of non-thermal states is attractive for transporting information and energy for long distances[44–46].

Methods

Hot-electron injection. We use custom-made voltage source and ammeter to inject hot electrons. A large input impedance of 100 kΩ in the ammeter prevents unwanted large current during adjustments. V_{Ginj} is precisely adjusted by a software to obtain the desired I_{inj} value (1 pA–1 nA) within a few % error before measuring I_{det} at each condition (V_{inj}, V_{G4}, etc.). V_{Ginj} depends strongly on V_{inj} (typically, from $V_{Ginj} \simeq -1.1$ V at $V_{inj} = 5$ mV to $V_{Ginj} \simeq -1.9$ V at $V_{inj} = 80$ mV with an almost linear relation in between) for $I_{inj} = 1$ nA. Slightly more negative V_{Ginj} by $\simeq -0.01$ V was needed for $I_{inj} = 10$ pA. While the location of the injector should be pushed toward the other gate G1 with more negative V_{Ginj}, we neglected possible change in transport length L. I_{inj} is kept sufficiently low, 1–10 pA for the QD detection to minimize the heating inside the QD and ~1 nA for the QPC detection for better visibility.

As the e–e scattering is sensitive to the distance from the channel to the gate metal, we fixed the gate voltages defining the channel ($V_{G1} = V_{G3} = -0.6$ V and $V_{G2} = -0.45$ V) throughout this paper. These gate voltages were chosen in such a way that the edge potential becomes gentle enough to suppress unwanted LO phonon emission while high enough to confine hot electrons[26,35,47]. While V_{inj} (1–100 meV) is much larger than the cyclotron energy of about 9 meV at 5 T, we did not observe any tunneling transition to higher Landau levels in the present conditions.

QPC detection. We focused on the current peaks appearing at the onsets of the conductance steps of the QPC, as described in the main text. Additional data that support our observation are shown in Supplementary Note 1. However, one can investigate the hot-electron energy from the current step appearing at $V_{G4} < -0.8$ V and $eV_{inj} > 30$ meV in Fig. 3b. This current step appears when the potential barrier height coincides with the hot-electron energy, as illustrated in the inset (iii) to Fig. 3a, and disappears at $eV_{inj} \lesssim 25$ meV in consistency with the hot spot condition obtained above. In our previous report, the hot-electron energy is obtained from V_{G4} at the current step by using a conversion factor determined from the LO phonon replicas of the current step[26,35]. The obtained λ in the range between 1 and 2 is consistent with the present value ($\lambda = 1.8$), while λ may depend on the device and the side gate voltage. However, the hot-electron energy cannot be obtained for the present case, as we suppressed LO phonon emission. Instead, the whole hot-electron energy is used for generating the electron-hole plasma, which is used to estimate p in this study.

QD detection. The QD characteristics ($U \simeq 1.5$ meV, $\bar{\Delta} \simeq 0.2$ meV, and $\alpha \simeq 0.044e$) were obtained from standard Coulomb diamond measurements at $V_{inj} = 0$ and $V_{Ginj} = 0$. The base electron temperature $T_B \simeq 110$ mK was also obtained from the onset of the CB peak. The backaction from the change in V_{Ginj} and V_{inj} to the detector conditions is present. While this is negligible for the QPC detection, the backaction to the QD is significant, as the CB peaks were shifted by ~30 mV in V_{G5} for $L = 1$ μm and ~8 mV for $L = 10$ μm when V_{inj} was changed from 1 to 90 mV under the adjustment of V_{Ginj} for $I_{inj} = 5$ pA. The relative value ΔV_{G5} from the CB peak is used in the main text. Additional data that support our observation are shown in Supplementary Note 2.

Analysis of the current profiles. We use the orthodox CB theory to analyze the broad current profile in the CB region at $\mu_N > \mu > \mu_D$ (see inset to Fig. 5a). As the current is sufficiently low, the dot should remain close to the base temperature. In this case, the tunneling rate from the edge channel of interest to the dot is given by $\Gamma_{dc} \simeq \int_{\mu_N}^{\infty} \frac{1}{e^2} G_L f(E) dE$ for the distribution function $f(E)$, where the tunneling conductance G_L may depends on energy. By assuming $T_B = 0$ for simplicity, the tunneling rates from the dot to the channel and drain read $\Gamma_{cd} \simeq \int_{\mu}^{\mu_N} \frac{1}{e^2} G_L dE$ and $\Gamma_{Dd} \simeq \int_{\mu_D}^{\mu_N} \frac{1}{e^2} G_R dE$, where G_L and G_R are tunneling conductances of the respective barriers. By solving the master equation, we obtain the steady current $I = e\Gamma_{dc}\Gamma_{Dd}/(\Gamma_{dc} + \Gamma_{Dd} + \Gamma_{cd})$. By assuming energy-dependent conductances $G_L \propto e^{E/W_t}$ and $G_R \propto e^{E/W_t}$ with the same characteristic energy W_t for the tunneling, we obtain $I \simeq \int_{\mu_N}^{\infty} \frac{1}{e} G_{QD} f(E) dE$ with $G_{QD} \propto e^{E/W_t}$ by neglecting factors that weakly depend on energy. This form was used in the analysis of distribution functions.

Data availability

The data and analysis used in this work are available from the corresponding author upon reasonable request.

References

1. Giamarchi, T. *Quantum Physics in One Dimension* (Oxford University Press, 2004).
2. Bäuerle, C. et al. Coherent control of single electrons: a review of current progress. *Rep. Prog. Phys.* **81**, 056503 (2018).
3. Tarucha, S., Honda, T. & Saku, T. Reduction of quantized conductance at low temperatures observed in 2 to 10 μm-long quantum wires. *Solid State Commun.* **94**, 413 (1995).
4. Bockrath, M. et al. Luttinger-liquid behaviour in carbon nanotubes. *Nature* **397**, 598 (1999).
5. Lorenz, T. et al. Evidence for spin-charge separation in quasi-one-dimensional organic conductors. *Nature* **418**, 614 (2002).
6. Auslaender, O. M. et al. Spin-charge separation and localization in one dimension. *Science* **308**, 88 (2005).
7. Ezawa, Z. F. *Quantum Hall Effects: Recent Theoretical and Experimental Developments* 3rd edn (World Scientific, 2013).
8. Chang, A. M. Chiral Luttinger liquids at the fractional quantum Hall edge. *Rev. Mod. Phys.* **75**, 1449 (2003).
9. Levkivskyi, I. *Mesoscopic Quantum Hall Effect (Springer Theses)* (Springer-Verlag, 2012).
10. von Delft, J. & Schoeller, H. Bosonization for beginners—refermionization for experts. *Ann. Phys.* **7**, 225 (1998).
11. Berg, E., Oreg, Y., Kim, E.-A. & von Oppen, F. Fractional charges on an integer quantum Hall edge. *Phys. Rev. Lett.* **102**, 236402 (2009).
12. Freulon, V. et al. Hong-Ou-Mandel experiment for temporal investigation of single-electron fractionalization. *Nat. Commun.* **6**, 6854 (2015).
13. Bocquillon, E. et al. Separation of neutral and charge modes in one-dimensional chiral edge channels. *Nat. Commun.* **4**, 1839 (2013).
14. Inoue, H. et al. Charge fractionalization in the integer quantum Hall effect. *Phys. Rev. Lett.* **112**, 166801 (2014).
15. Kamata, H., Kumada, N., Hashisaka, M., Muraki, K. & Fujisawa, T. Fractionalized wave packets from an artificial Tomonaga–Luttinger liquid. *Nat. Nanotech.* **9**, 177 (2014).
16. Hashisaka, M., Hiyama, N., Akiho, T., Muraki, K. & Fujisawa, T. Waveform measurement of charge- and spin-density wavepackets in a chiral Tomonaga–Luttinger liquid. *Nat. Phys.* **13**, 559 (2017).
17. Gutman, D. B., Gefen, Y. & Mirlin, A. D. Bosonization of one-dimensional fermions out of equilibrium. *Phys. Rev. B* **81**, 085436 (2010).

18. Gutman, D. B., Gefen, Y. & Mirlin, A. D. Nonequilibrium Luttinger liquid: zero-bias anomaly and dephasing. *Phys. Rev. Lett.* **101**, 126802 (2008).

19. Iucci, A. & Cazalilla, M. A. Quantum quench dynamics of the Luttinger model. *Phys. Rev. A* **80**, 063619 (2009).

20. Kovrizhin, D. L. & Chalker, J. T. Equilibration of integer quantum Hall edge states. *Phys. Rev. B* **84**, 085105 (2011).

21. Levkivskyi, I. P. & Sukhorukov, E. V. Energy relaxation at quantum Hall edge. *Phys. Rev. B* **85**, 075309 (2012).

22. Washio, K. et al. Long-lived binary tunneling spectrum in the quantum Hall Tomonaga-Luttinger liquid. *Phys. Rev. B* **93**, 075304 (2016).

23. Itoh, K. et al. Signatures of a nonthermal metastable state in copropagating quantum Hall edge channels. *Phys. Rev. Lett.* **120**, 197701 (2018).

24. Rodriguez, R. H. et al. Relaxation and revival of quasiparticles injected in an interacting quantum Hall liquid. *Nat. Commun.* **11**, 2426 (2020).

25. Taubert, D. et al. Relaxation of hot electrons in a degenerate two-dimensional electron system: transition to one-dimensional scattering. *Phys. Rev. B* **83**, 235404 (2011).

26. Ota, T., Akiyama, S., Hashisaka, M., Muraki, K. & Fujisawa, T. Spectroscopic study on hot-electron transport in a quantum Hall edge channel. *Phys. Rev. B* **99**, 085310 (2019).

27. Fletcher, J. D. et al. Clock-controlled emission of single-electron wave packets in a solid-state circuit. *Phys. Rev. Lett.* **111**, 216807 (2013).

28. Kataoka, M. et al. Time-of-flight measurements of single-electron wave packets in quantum Hall edge states. *Phys. Rev. Lett.* **116**, 126803 (2016).

29. Johnson, N. et al. LO-phonon emission rate of hot electrons from an on demand single-electron source in a GaAs/AlGaAs heterostructure. *Phys. Rev. Lett.* **121**, 137703 (2018).

30. Fletcher, J. D. et al. Continuous-variable tomography of solitary electrons. *Nat. Commun.* **10**, 5298 (2019).

31. Ubbelohde, N. et al. Partitioning of on-demand electron pairs. *Nat. Nanotech.* **10**, 46 (2014).

32. Khodas, M., Pustilnik, M., Kamenev, A. & Glazman, L. I. Fermi-Luttinger liquid: spectral function of interacting one-dimensional fermions. *Phys. Rev. B* **76**, 155402 (2007).

33. Lunde, A. M., Nigg, S. E. & Büttiker, M. Interaction-induced edge channel equilibration. *Phys. Rev. B* **81**, 041311 (2010).

34. Lunde, A. M. & Nigg, S. E. Statistical theory of relaxation of high-energy electrons in quantum Hall edge states. *Phys. Rev. B* **94**, 045409 (2016).

35. Akiyama, S. et al. Ballistic hot-electron transport in a quantum Hall edge channel defined by a double gate. *Appl. Phys. Lett.* **115**, 243106 (2019).

36. Altimiras, C. et al. Non-equilibrium edge-channel spectroscopy in the integer quantum Hall regime. *Nat. Phys.* **6**, 34 (2010).

37. Nazarov, Y. V. & Blantar, Y. M. *Quantum Transport: Introduction to Nanoscience* (Cambridge University Press, 2009).

38. Altshuler, B. L. & Aronov, A. G. Electron-electron interaction in disordered conductors. In *Electron-Electron Interactions in Disordered Systems* (eds Efros, A. L. & Pollak, M.) 1 (North-Holland Physics Publishing, 1985).

39. Pothier, H., Guéron, S., Birge, N. O., Esteve, D. & Devoret, M. H. Energy distribution function of quasiparticles in mesoscopic wires. *Phys. Rev. Lett.* **79**, 3490 (1997).

40. Jezouin, S. et al. Quantum limit of heat flow across a single electronic channel. *Science* **342**, 601–604 (2013).

41. le Sueur, H. et al. Energy relaxation in the integer quantum Hall regime. *Phys. Rev. Lett.* **105**, 056803 (2010).

42. Prokudina, M. G. et al. Tunable nonequilibrium Luttinger liquid based on counterpropagating edge channels. *Phys. Rev. Lett.* **112**, 216402 (2014).

43. Imambekov, A., Schmidt, T. L. & Glazman, L. I. One-dimensional quantum liquids: beyond the Luttinger liquid paradigm. *Rev. Mod. Phys.* **84**, 1253 (2012).

44. Calzona, A., Gambetta, F. M., Cavaliere, F., Carrega, M. & Sassetti, M. Quench-induced entanglement and relaxation dynamics in Luttinger liquids. *Phys. Rev. B* **96**, 085423 (2017).

45. Kaminishi, E., Mori, T., Ikeda, T. N. & Ueda, M. Entanglement prethermalization in the Tomonaga-Luttinger model. *Phys. Rev. A* **97**, 013622 (2018).

46. Ueda, M. Quantum equilibration, thermalization and prethermalization in ultracold atoms. *Nat. Rev. Phys.* **2**, 669 (2020).

47. Emary, C., Clark, L. A., Kataoka, M. & Johnson, N. Energy relaxation in hot electron quantum optics via acoustic and optical phonon emission. *Phys. Rev. B* **99**, 045306 (2019).

Acknowledgements

Author contributions

T.F. designed and supervised this study. T.A. and K.M. grew the wafer. Y.S. fabricated the device. K.S. performed the measurement and analysis with help from T.H. and T.F. K.S. and T.F. wrote the manuscript. All authors discussed the results and commented on the manuscript.

Competing interests

The authors declare no competing interests.

Additional information

Supplementary information The online version contains supplementary material available at https://doi.org/10.1038/s42005-023-01223-y.

Correspondence and requests for materials should be addressed to Toshimasa Fujisawa.

Peer review information *Communications Physics* thanks the anonymous reviewers for their contribution to the peer review of this work.

Reprints and permission information is available at http://www.nature.com/reprints

Publisher's note Springer Nature remains neutral with regard to jurisdictional claims in published maps and institutional affiliations.